ACS OMEGA

http://pubs.acs.org/journal/acsodf

Article

Synthesis of Porphyrin Zr-MOFs for the Adsorption and Photodegradation of Antibiotics under Visible Light

Yuqing Zong,[§] Shuaishuai Ma,[§] Jiamin Gao, Minjing Xu, Jinjuan Xue,* and Mingxin Wang*

Cite This: *ACS Omega* 2021, 6, 17228−17238

Read Online

ACCESS | Metrics & More | Article Recommendations

ABSTRACT: The release of antibiotics into the water environment can pose a serious threat to human and ecological health, so it is of great significance to effectively remove antibiotics from wastewater. In this work, porphyrinic zirconium metal−organic framework material, PCN-224, was first explored for the adsorption removal of antibiotics from water using tetracycline (TC) and ciprofloxacin (CIP) as examples. We prepared a series of PCN-224 with different particle sizes (150 nm, 300 nm, 500 nm, and 6 μm). Benefiting from the huge surface area (1616 $m^2\ g^{-1}$), the 300 nm-PCN-224 sample had the best adsorption properties for TC and CIP. Remarkably, it exhibits fast removal rates and high adsorption capacities of 354.81 and 207.16 mg g^{-1} for TC and CIP, respectively. The adsorption of TC and CIP in 300 nm-PCN-224 is consistent with the pseudo-second-order kinetic model and Langmuir isotherm model, which indicates that the adsorption can be regarded as homogeneous monolayer chemisorption, and the adsorption is exothermic, which has been confirmed by thermodynamic studies. Under visible-light irradiation, 300 nm-PCN-224 exhibited high photocatalytic activity for TC and CIP. The adsorption studies confirmed that the adsorption of adsorbates takes place via the formation of hydrogen bonding, $\pi-\pi$ interactions, and electrostatic attraction. In addition, the adsorbent can be simply regenerated by photocatalysis under visible light, and the adsorption−desorption efficiency is still above 85% after repeated use five times. The work of MOFs to remove antibiotics from water shows that MOFs have great potential in this field and are worthy of further study.

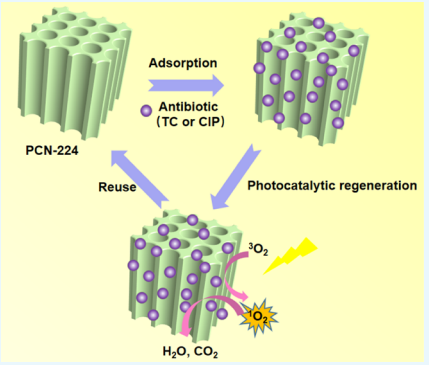

1. INTRODUCTION

In the past century, antibiotics have been widely used in human clinical, animal husbandry, aquaculture, and other fields, playing an important role in the treatment of infectious diseases.[1−3] However, since most antibiotics cannot be completely metabolized in the human body or biodegraded in the natural environment, the potential risk of antibiotic abuse has been paid more and more attention.[4−6] Antibiotics are frequently detected in the effluent of wastewater treatment plants, surface water, and groundwater.[6−9] Residues of these antibiotics can induce the production of drug-resistant bacteria and affect biological metabolism, posing a threat to human and ecological health.[10−12] Therefore, necessary measures must be taken to prevent arbitrary exposure of antibiotics in the aquatic environment, and the adsorption method is currently known as one of the most effective methods for removing various organic pollutants in water because it has advantages in terms of operating cost, simplicity, removal efficiency, and practicality.[13,14] Various adsorbents such as activated carbon, carbon nanotubes, graphene oxide, biochar, porous silica, molecularly imprinted polymers, porous resins, and metal oxides have been used to adsorb and remove antibiotics.[15−21] However, the regeneration of adsorbents and the disposal of adsorbed antibiotics are still a problem. Therefore, it is necessary to develop new materials with high adsorption capacity and multifunctional combinations to effectively remove residues of antibiotics in water.

Meta−organic frameworks (MOFs) are a kind of porous organic−inorganic hybrid material formed by self-assembly of metal ions or metal clusters and organic ligands.[22,23] Due to their high porosity, controllable pore size/shape, and unique physicochemical properties, MOFs materials have proven their usefulness in a variety of applications, including gas storage, separation, sensors and catalysis.[24−27] However, most MOF-based adsorbents show disadvantages in water treatment due to their poor water stability, small pore size, and difficulty in regeneration. PCN-224 is a porphyrin MOF composed of $Zr_6O_4(OH)_4$ cluster and organic porphyrin ligand (TCPP), which has high biocompatibility, excellent photovoltaic activity, and environmental stability.[28,29] Because of the presence of porphyrin, this kind of MOF can be triggered by 660 nm light to produce reactive oxygen species (ROS). The

Received: February 19, 2021
Accepted: May 24, 2021
Published: June 29, 2021

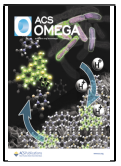

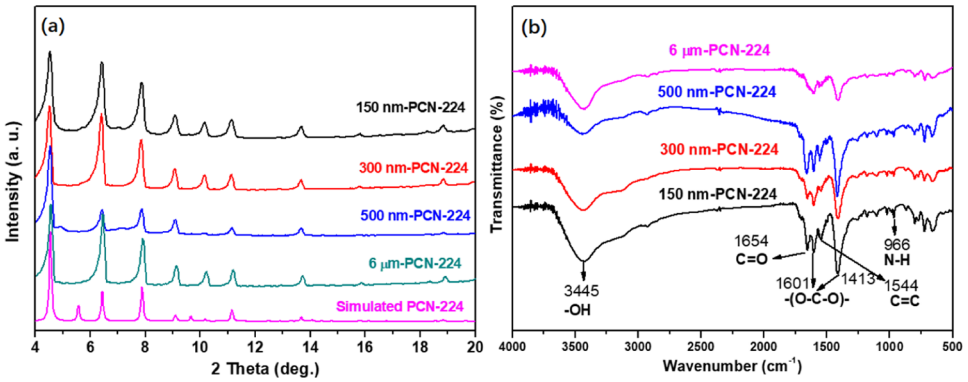

Figure 1. (a) XRD patterns for simulated and experimental PCN-224 samples. (b) FT-IR spectra of PCN-224 series.

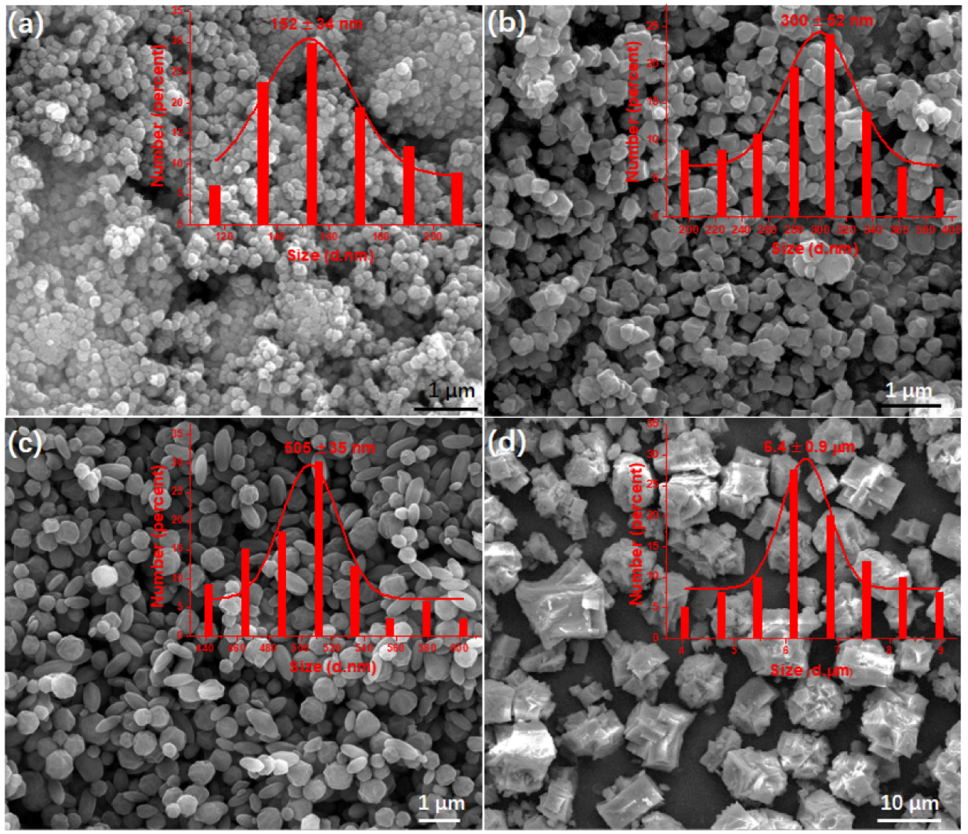

Figure 2. FESEM images of (a) 150 nm-PCN-224, (b) 300 nm-PCN-224, (c) 500 nm-PCN-224, (d) 6 μm-PCN-224, and size distribution of PCN-224 nanoparticles by FESEM (inset).

resulting ROS is capable of decomposing organic pollutants, which means that PCN-224 can eliminate adsorbates and achieve in situ regeneration.[30,31] Therefore, the water stability, high porosity, relatively large pore size, and photoactivity of PCN-224 make it a potential water treatment material. However, to the best of our knowledge, the adsorption performance of PCN-224 for antibiotics and the photocatalytic regeneration of the adsorbent has not been studied.

Inspired by the above-mentioned points, we herein present an investigation of both adsorption and visible light degradation of antibiotic residues in water based on PCN-224. Tetracycline (TC) and ciprofloxacin (CIP) were selected as representatives of antibiotics for experimental study. The effects of adsorption kinetics, thermodynamics, isotherms, pH value, and ionic strength were systematically studied. In addition, the photocatalytic performance of PCN-224 was studied experimentally and the reusability of PCN-224 was tested for a potential application.

2. RESULTS AND DISCUSSION

The crystalline structures of the PCN-224 series were confirmed by X-ray diffraction (XRD) patterns. As shown in Figure 1a, 150 nm-PCN-224, 300 nm-PCN-224, 500 nm-PCN-224, and 6 μm-PCN-224 show sharp crystalline diffraction peaks at 4.52, 6.42, 7.84, 9.06, 11.16, and 13.68°, which represent the crystal planes (002), (022), (222), (004), (224), and (006), respectively, in good agreement with those observed for simulated PCN-224, demonstrating the successful synthesis of PCN-224.[32,33] The Fourier transform infrared (FT-IR) spectra of the PCN-224 samples are depicted in

https://doi.org/10.1021/acsomega.1c00919
ACS Omega 2021, 6, 17228−17238

Figure 1b. The intensities of the asymmetric vibrational absorption at 1654 cm^{-1} can be ascribed to C═O groups from H_2TCPP.[34] The peak near 1544 cm^{-1} is favored by the C═C stretching vibration. The wide signal located at 3445 cm^{-1} is assigned to the O−H vibrations, demonstrating the presence of bonding and free water in all prepared samples. The peak situated at 966 cm^{-1} is attributed to the N−H bond adsorbs vibration.[35] The vibrational bands around 1413 and 1601 cm^{-1} are characteristic of the framework −(O−C−O)− groups, which confirms the presence of the dicarboxylate within the product.[30]

The morphology and microstructure of the prepared samples were determined by the field emission scanning electron microscopy (FESEM) technique. As shown in Figure 2a, 150 nm-PCN-224 nanoparticles exhibited uniform morphology while displaying egregious agglomeration, which showed an average size of around 150 nm (Figure 1a inset). The as-obtained 300 nm-PCN-224 sample showed a well-defined cubic-like morphology with an average size of about 300 nm (Figure 2b and inset). Figure 2c displays a representative FESEM image of 500 nm-PCN-224. It can be observed that the crystals are regular almond-like nanoparticles and the average diameter is about 500 nm (Figure 2c inset). For 6 μm-PCN-224 (Figure 2d), these sharp-edged crystals have a cubic appearance with the average crystallite size ranging from 4 to 10 μm.

The specific surface area and porous nature of the as-prepared PCN-224 samples were analyzed by the N_2 adsorption−desorption technique (Figure 3). For all tested

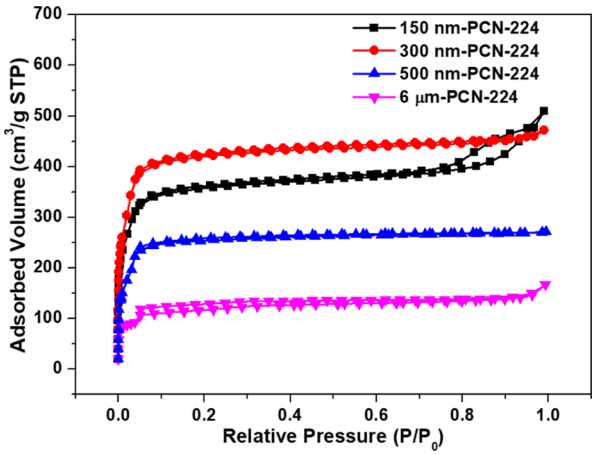

Figure 3. N_2 adsorption−desorption isotherms of the as-prepared PCN-224 series.

samples, the isotherms increased rapidly at $P/P_0 < 0.1$, denoting the existence of micropores. However, 150 nm-PCN-224 displayed a type IV isotherm with an H3 hysteresis loop at a relatively high pressure range, indicating that it had a mesoporous morphology and was derived from the seriously agglomerated 150 nm-PCN-224 nanoparticles.[34,36] Other physical parameters, including the specific surface area (SSA), single point total pore volume (V_{tot}), and micropore volume (V_{micro}), were calculated and are shown in Table 1. The surface area of 300 nm-PCN-224 was 1349 $m^2\ g^{-1}$, which is higher than those of the other three 150 nm-PCN-224 (1349 $m^2\ g^{-1}$), 500 nm-PCN-224 (954 $m^2\ g^{-1}$), and 6 μm-PCN-224 (431 $m^2\ g^{-1}$). Moreover, the calculated total pore volume and the micropore volume of 300 nm-PCN-224 were as high as

Table 1. Specific Surface Area, Single Point Total Pore Volume, and Micropore Volume of the As-Prepared PCN-224 Samples

samples	SSA[a] ($m^2\ g^{-1}$)	V_{tot}[b] ($cm^3\ g^{-1}$)	V_{micro}[c] ($cm^3\ g^{-1}$)
150 nm-PCN-224	1349	0.789	0.437
300 nm-PCN-224	1616	0.729	0.537
500 nm- PCN-224	954	0.419	0.326
6 μm-PCN-224	431	0.259	0.116

[a]Specific surface area. [b]Single point total pore volume. [c]Micropore volume.

0.729 and 0.537 $cm^3\ g^{-1}$, respectively. The high specific surface area is conducive to the adsorption and transfer of pollutant molecules, and thus also benefits the catalytic performance.

To compare the adsorption capacities of the four materials, tests were carried out under the following conditions: initial TC or CIP concentration = 10 mg L^{-1}, adsorbent dosage = 0.5 g L^{-1}, T = 298 K, and pH = 7.0. As observed from Figure 4a, with the increase of particle size (150−300 nm), the adsorption capacity of 300 nm-PCN-224 showed an increasing trend, which was related to the disappearance of agglomeration and the increase of specific surface area. Particularly, the removal rate of TC increased from 65.2 to 99.1% within 4 min. However, when the particle size reached 500 nm or larger, the adsorption performance of PCN-224 decreased dramatically under the same conditions, which may be related to the sharp decrease of the specific surface area. Meanwhile, it can be seen from Figure 4b that the removal efficiency of PCN-224 series samples for CIP also shows the same trend as TC, but the removal efficiency is slightly reduced. This may be because TC contains more functional groups than CIP for bonding, which resulted in a greater adsorption affinity of PCN-224 to TC than that to CIP. Therefore, 300 nm-PCN-224 was used for further adsorption isotherm and kinetics study.

The kinetics of TC and CIP adsorption onto 300 nm-PCN-224 were fitted to the pseudo-first-order kinetic, pseudo-second-order kinetic, and intraparticle diffusion kinetic models using the following equations

The pseudo-first-order model

$$\ln(q_e - q_t) = \ln q_e - k_1 t \quad (1)$$

The pseudo-second-order kinetic model

$$\frac{t}{q_t} = \frac{1}{k_2 q_e^2} + \frac{t}{q_e} \quad (2)$$

The intraparticle diffusion kinetic models

$$q_t = k_i t^{1/2} \quad (3)$$

where k_1, k_2, and k_i are the kinetic rate constants. The fitting results and kinetic parameters are shown in Figure 5 and Table 2. Based on Figure 5a,b,d,e and Table 2, the correlation coefficients of the pseudo-second-order model (R^2 = 0.9999 (TC), 0.9999 (CIP)) was much higher than those of the pseudo-first-order model (R^2 = 0.7439 (TC), 0.4288 (CIP)), revealing that it could describe the adsorptive behavior better, indicating that chemisorption might play a dominant role in adsorption reactions.[37] In addition, the experimental adsorption capacity ($q_{e,exp}$) agreed better with the calculated adsorption capacity ($q_{e,cal}$) using the pseudo-second-order model. To better understand the adsorption kinetics of 300 nm-PCN-224 for TC or CIP, the intraparticle diffusion kinetic

https://doi.org/10.1021/acsomega.1c00919
ACS Omega 2021, 6, 17228−17238

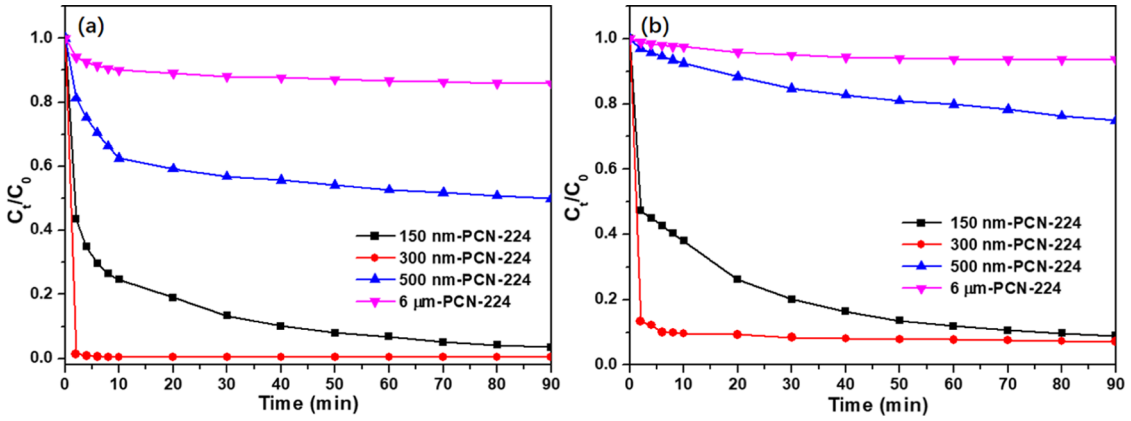

Figure 4. Removal efficiency of (a) TC and (b) CIP by adsorbent.

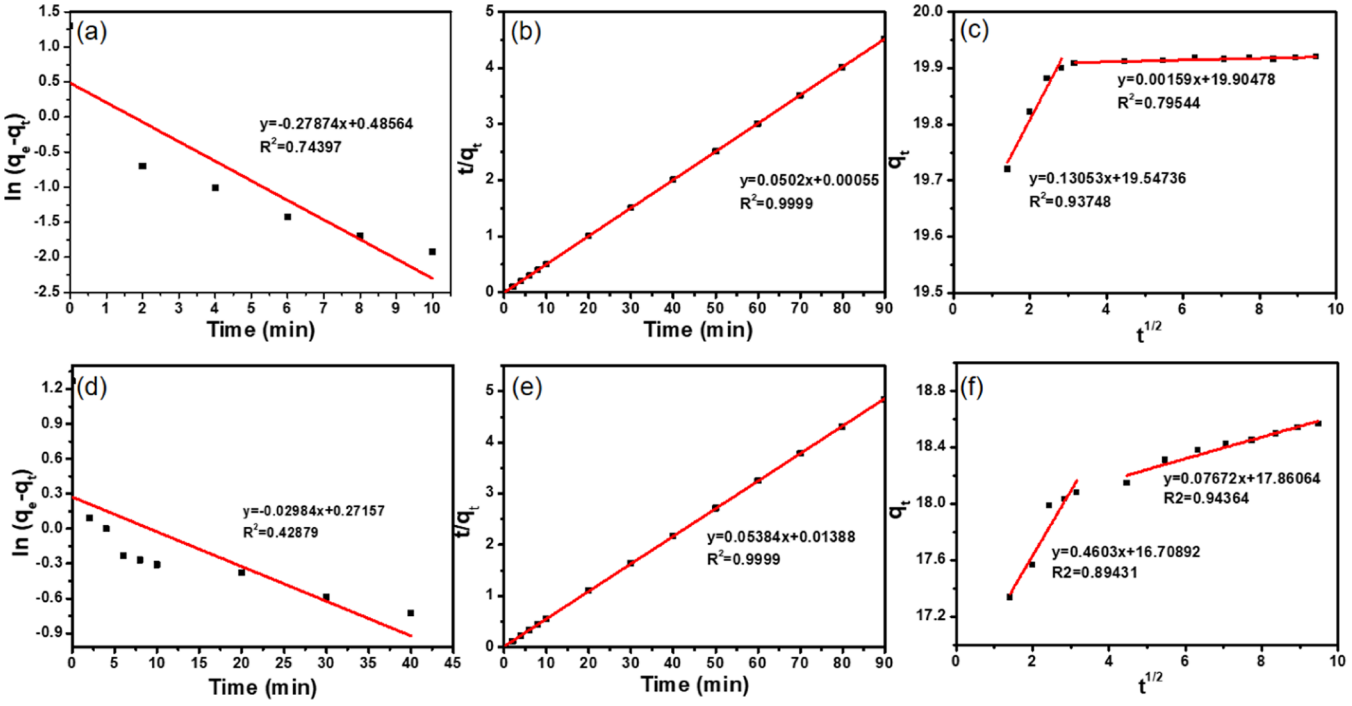

Figure 5. Pseudo-first-order, pseudo-second-order, and intraparticle diffusion model of TC (a−c) and CIP (d−f) adsorption on 300 nm-PCN-224.

Table 2. Kinetic Parameters for TC and CIP Adsorption on 300 nm-PCN-224

			pseudo-first-order model			pseudo-second-order model		
pollutants	sample	q_{exp} (mg g^{-1})	k_1 (min^{-1})	$q_{e,cal}$ (mg g^{-1})	R^2	k_2 (g mg^{-1} min^{-1})	$q_{e,cal}$ (mg g^{-1})	R^2
TC	300 nm-PCN-224	19.92	2.351	19.89	0.7439	2.407	19.93	0.9999
CIP	300 nm-PCN-224	18.57	1.454	18.26	0.4288	0.361	18.54	0.9999

model was employed to fit the experimental kinetic data. As shown in Figure 5c,f, the fitting area was divided into two parts. The first part fitted a straight line with a steep slope as a fast adsorption process. The second part had a gradual slope, indicating that the adsorption equilibrium changed slowly with time.[38] However, the fitted line did not pass through the origin, which showed that the rate-limiting step was not controlled by the intraparticle diffusion.[39]

Adsorption isotherms can reflect the surface properties and the affinity of adsorbents. Therefore, to evaluate the adsorption performance of 300 nm-PCN-224, the isotherm models of classic Langmuir eq 4 and Freundlich eq 5 were applied for data simulation.

$$q_e = \frac{q_m K_L C_e}{1 + C_e K_L} \quad (4)$$

$$q_e = K_F C_e^{1/n} \quad (5)$$

where q_m is the maximum adsorptive capacity of adsorbents. K_L and K_F are the Langmuir and the Freundlich constants, respectively. The empirical constant n indicates a heterogeneity factor. These simulated parameters are presented in Figure 6 and Table 3. The correlation coefficient for the linear plots in

https://doi.org/10.1021/acsomega.1c00919
ACS Omega 2021, 6, 17228−17238

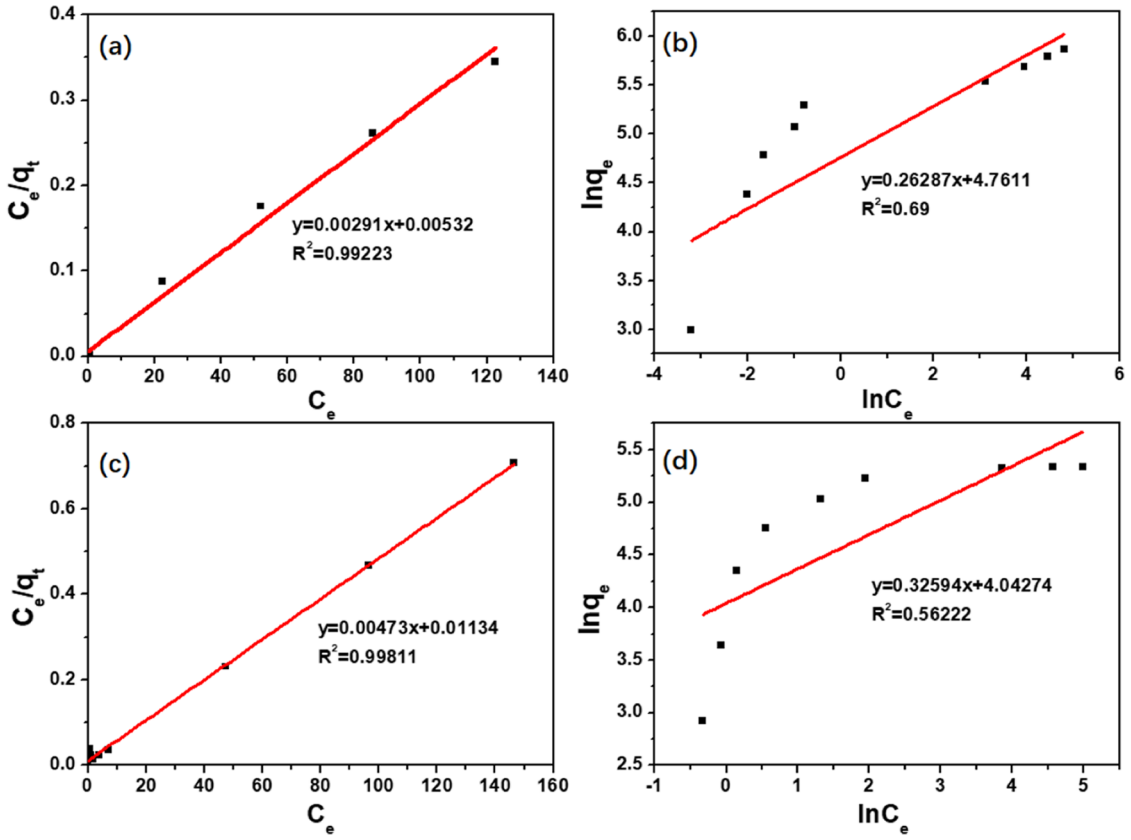

Figure 6. Langmuir and Freundlich isotherm models for TC (a, b) and CIP (c, d) adsorption on 300 nm-PCN-224.

Table 3. Langmuir and Freundlich Parameters for the Adsorption of TC and CIP onto 300 nm-PCN-224

model	parameters	TC	CIP
Langmuir	q_m (mg g^{-1})	338	208
	K_L (L mg^{-1})	2.668	0.4566
	R^2	0.9922	0.9981
Freundlich	K_F ($mg^{1-1/n}$ L^{-1} g^{-1})		
	n		
	R^2	0.69	0.5622

the Langmuir model is closer to 1 (R^2 = 0.9923 (TC), 0.9981 (CIP)) compared to that in the Freundlich model (R^2 = 0.69 (TC), 0.5622 (CIP)). Thereby, the Langmuir isotherm should be selected as the most suitable isotherm model to describe the adsorption equilibrium behavior of TC or CIP on the surface of 300 nm-PCN-224. This result indicated that the monolayer adsorption occurs at 300 nm-PCN-224 in a limited number of equal sites.[40] Therefore, it was predicted that increasing their surface area would increase the volume of the binding sites, thus improving their adsorption capacity for TC and CIP. Moreover, the maximum adsorption capacities of 300 nm-PCN-224 for TC and CIP calculated from the Langmuir model were 338 and 208 mg g^{-1}, respectively, which approached the experimental values shown in Figure 7. The results displayed a very high adsorption capacity toward antibiotics than various adsorbents from the reported literature (Table 4).

The thermodynamic parameters provide in-depth information regarding the inherent energetic changes connected with adsorption. Gibbs free energy (ΔG^0), enthalpy (ΔH^0), and entropy (ΔS^0) were calculated by the following equation

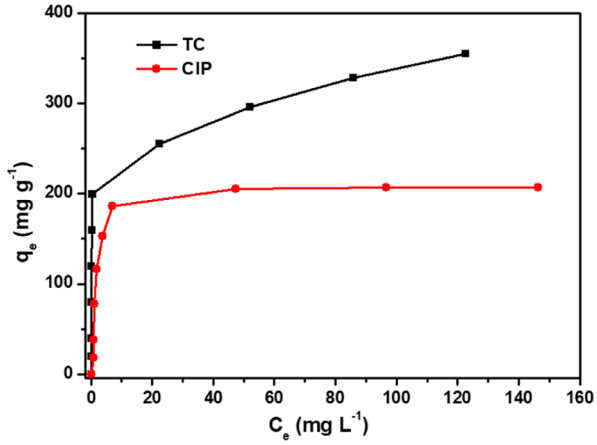

Figure 7. Adsorption isotherm curve of 300 nm-PCN-224 for TC and CIP.

$$\ln K^0 = \frac{\Delta S^0}{R} - \frac{\Delta H^0}{RT} \quad (6)$$

$$K^0 = \frac{q_e}{C_e} \quad (7)$$

$$\Delta G^0 = -RT \ln K^0 \quad (8)$$

where T is the absolute temperature (K), K^0 is the adsorption equilibrium constant, and R is the gas constant (8.314 J mol^{-1} K^{-1}). According to Figure 8 and Table 5, the negative values of ΔG^0 recommended that the adsorption of TC and CIP onto 300 nm-PCN-224 was spontaneous and thermodynamically favorable. The negative ΔH^0 values indicated that the

https://doi.org/10.1021/acsomega.1c00919
ACS Omega 2021, 6, 17228−17238

Table 4. Comparison of Adsorption Capacity of Adsorbates with Previously Reported Adsorbents

s. no.	adsorbent	adsorbate	surface area (m^2 g^{-1})	adsorption capacity (mg g^{-1})	refs
1.	Fe_3O_4/C	ciprofloxacin	23.6	98.28	41
2.	ball-milled (BCFS) crayfish shell biochar	tetracycline	289.7	60.7	42
3.	carbon-doped boron nitride (BCN)	tetracycline	18.708	76.74	43
4.	SiO_2 Nanoparticles	ciprofloxacin	190	59.28	44
5.	TiO_2(B) @carbon composites	tetracycline	49.26	190	45
6.	carbon nanotubes	ciprofloxacin	135	284	46
7.	mesoporous BiOI microspheres	tetracycline	28.35	28.1	47
8.	300 nm-PCN-224	tetracycline ciprofloxacin	338, 208	1616	this work

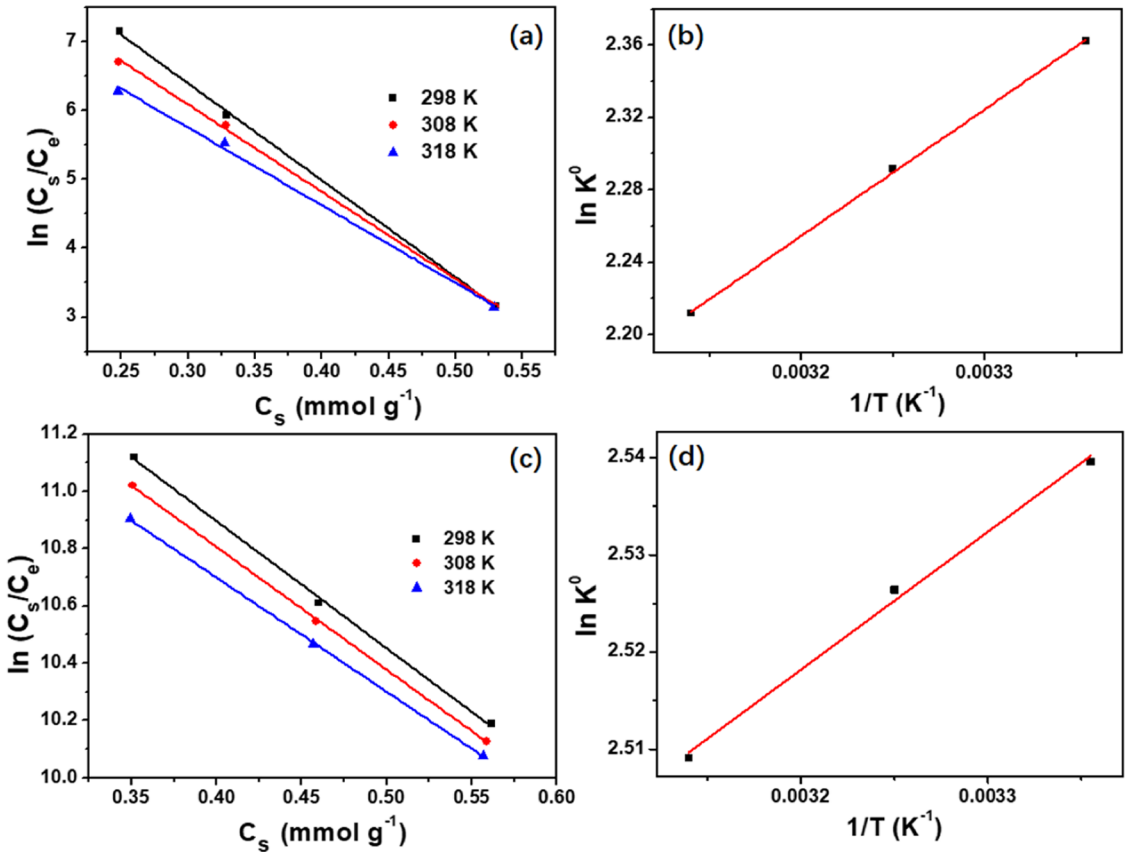

Figure 8. Plots of $\ln(C_s/C_e)$ and C_s and $\ln K^0$ versus $1/T$ for the adsorption of TC (a, b) and CIP (c, d) on 300 nm-PCN-224.

Table 5. Thermodynamic Parameters of TC and CIP onto 300 nm-PCN-224

pollutants	ΔH^0 (kJ mol^{-1})	ΔS^0 (J mol^{-1} K^{-1})	T (K)	K^0	ΔG^0 (kJ mol^{-1})	R^2
TC	−5.819	0.125	298	10.615	−5.852	0.999
			308	9.890	−5.867	0.998
			318	9.133	−5.848	0.995
CIP	−1.181	17.157	298	12.675	−6.292	0.997
			308	12.521	−6.472	0.999
			318	12.294	−6.634	0.999

adsorption process of TC and CIP was exothermic. In other words, a lower adsorption temperature promotes the adsorption property of 300 nm-PCN-224. Besides, the degree of the disorder increased at the adsorbent−adsorbate interface on account of ΔS being greater than 0.[48,49]

The pH value of the solution determines the surface charge of the adsorbent and the adsorbent, which causes the electrostatic interaction between the adsorbent and the adsorbent. To determine the effect of pH, experiments were conducted at different initial pH values. As shown in Figure 9a, 300 nm-PCN-224 exhibits good adsorption performance in the pH range (3−9), and the adsorption capacity reaches the maximum at pH (7), which is considered to be the ideal pH for removing TC and CIP. When the pH exceeds 9, the structure of PCN-224 is unstable and the adsorption capacity is significantly reduced.[50] In fact, the composition of actual wastewater is complicated because of the large number of compounds in it. To study the effect of ionic strength on the adsorption of TC and CIP on 300 nm-PCN-224, different amounts of NaCl were added to the solution, and the results

https://doi.org/10.1021/acsomega.1c00919
ACS Omega 2021, 6, 17228−17238

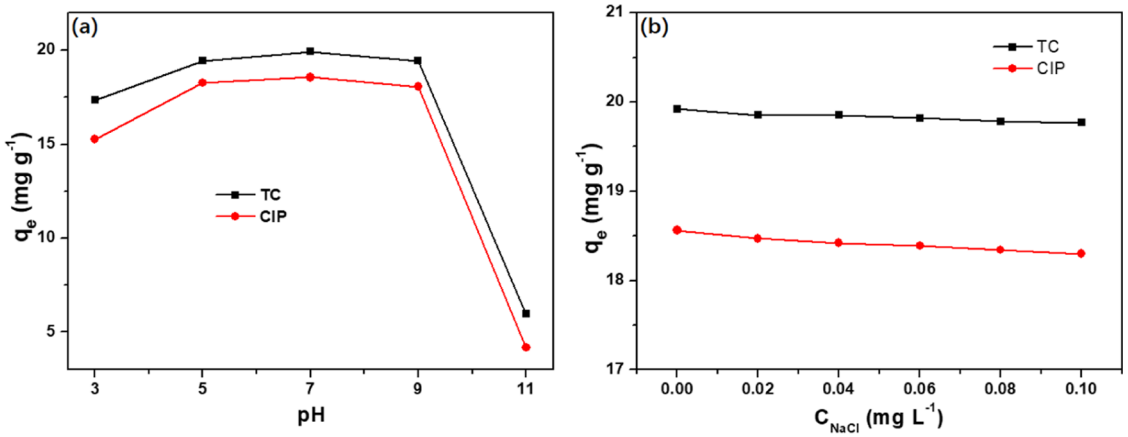

Figure 9. Effect of (a) pH and (b) NaCl concentration on the adsorption of TC and CIP onto 300 nm-PCN-224.

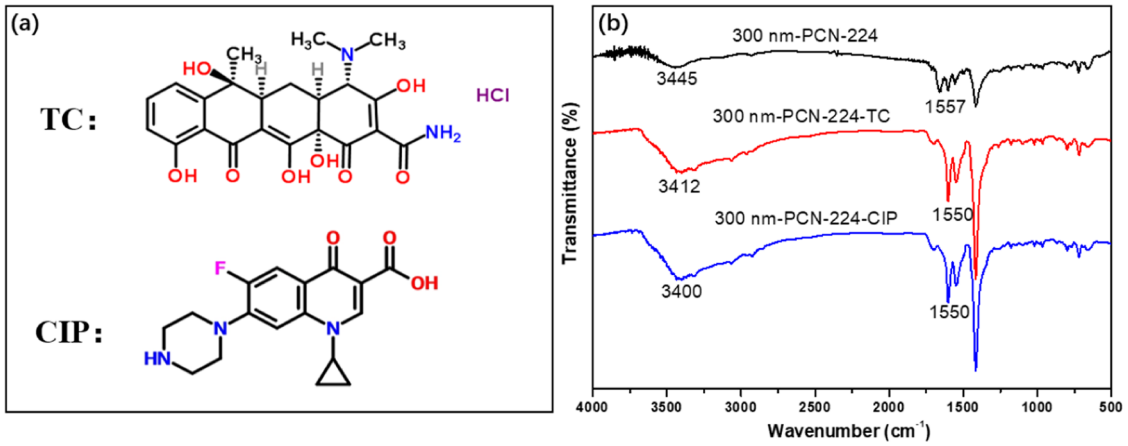

Figure 10. Structural formulas of the two antibiotics (a) and FT-IR of the 300 nm-PCN-224 before and after adsorption (b).

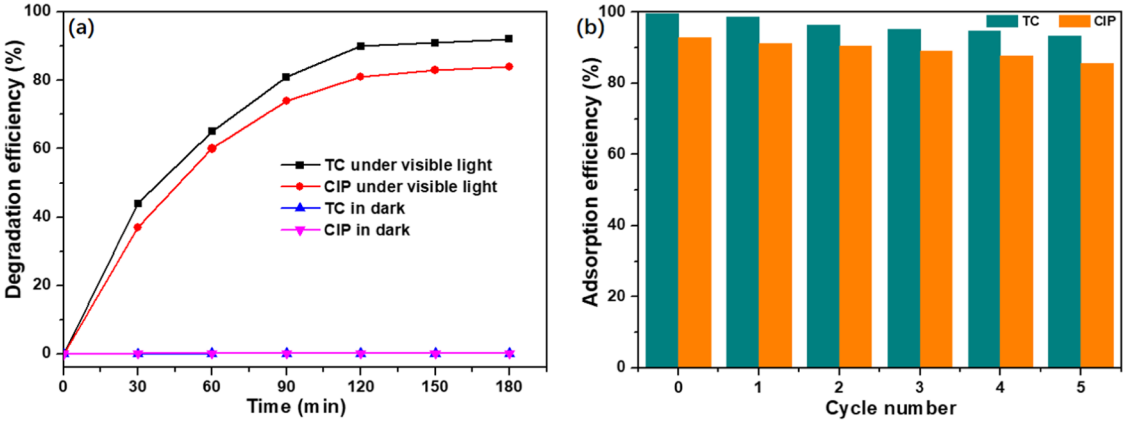

Figure 11. Photocatalytic regeneration (a) and reusability (b) of 300 nm-PCN-224.

are shown in Figure 9b. In terms of ionic strength, the adsorption properties of 300 nm-PCN-224 for TC and CIP did not change significantly with the increase of NaCl concentration, indicating that 300 nm-PCN-224 has a good anti-interference ability against salt ions in a solution, which may be due to the electrostatic interaction between 300 nm-PCN-224 and NaCl.[51]

The kinetic analysis suggests a key role of chemisorption in the CIP and TC adsorption by 300 nm-PCN-224. The variations of adsorption amount at different pH values showed that the electrostatic attraction contributed to antibiotic adsorption. The benzene rings in TC and CIP (Figure 10a) can interact with the porphyrin macrocycles in 300 nm-PCN-224 through $\pi-\pi$ stacking interaction. As shown in Figure 10b, the FT-IR spectra analyses of 300 nm-PCN-224 before and after adsorption are shown in Figure 10. The FT-IR peaks of the −OH group shifted from 3445 to 3412 and 3400 cm^{-1} after adsorption, suggesting the existence of H-bonding interactions.[52] The shifting of the peak was also observed from 1557 to 1550 cm^{-1} for aromatic C=C groups, indicating the possibility of $\pi-\pi$ interactions.[53] Based on the above analysis, it can be concluded that the adsorption of TC and

https://doi.org/10.1021/acsomega.1c00919
ACS Omega 2021, 6, 17228−17238

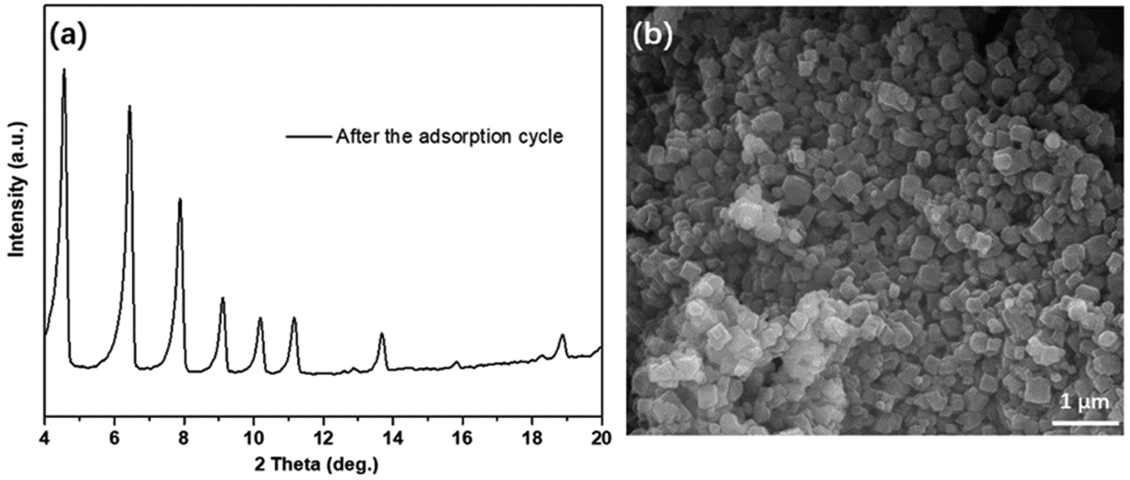

Figure 12. XRD pattern (a) and FESEM image (b) of 300 nm-PCN-224 samples after the adsorption cycle.

CIP molecule on 300 nm-PCN-224 is predominantly through electrostatic attraction, hydrogen bonding, and $\pi-\pi$ interactions.

To prove the photocatalytic regeneration performance of 300 nm-PCN-224, photodegradation experiments of TC and CIP were performed under visible-light irradiation after the adsorption process, and the results are illustrated in Figure 11a. In the control experiment, the concentrations of TC and CIP in the eluent did not change in the absence of visible-light irradiation. However, the concentration of TC and CIP in the eluent decreased significantly under visible-light irradiation, and the removal rates of TC and CIP could reach 92 and 84% (in 180 min), respectively, indicating that 300 nm-PCN-224 could effectively degrade TC and CIP under visible light, showing excellent photocatalytic regeneration performance. This is because the porphyrin moieties in 300 nm-PCN-224 were excited by visible light to yield reactive oxygen species, and the adsorbed TC and CIP on 300 nm-PCN-224 were then degraded by the produced singlet oxygen.[30,54] To investigate the reusability of the adsorbent, the 300 nm-PCN-224 sample after adsorption and photocatalysis was reused five times under the same conditions. As shown in Figure 11b, 300 nm-PCN-224 displays good recyclability in terms of TC and CIP removal during five cycles. Also, after five cycles of experiments, the XRD crystal phase (Figure 12a) and SEM image (Figure 12b) of 300 nm-PCN-224 showed that the crystal phase and morphology of the sample did not change significantly. The porosity of 300 nm-PCN-224 decreased from the original 0.729 to 0.683 $cm^3\ g^{-1}$. This may be caused by the accumulation of intermediate products produced in the photocatalytic degradation process, or by antibiotic residues. The results show that the material has good chemical stability and is a promising adsorbent for the effective removal of TC and CIP from an aqueous solution.

To prove that PCN-224 can produce $^1O_2$ under visible irradiation, 1,3-diphenylisobenzofuran (DPBF) bleaching experiment was performed, and the results are illustrated in Figure 13. DBPF with fluorescent color is gradually oxidized to colorless 1,2-dibenzoylbenzene, with the color of the solution gradually becoming lighter, and the absorbance at 415 nm is decreased.

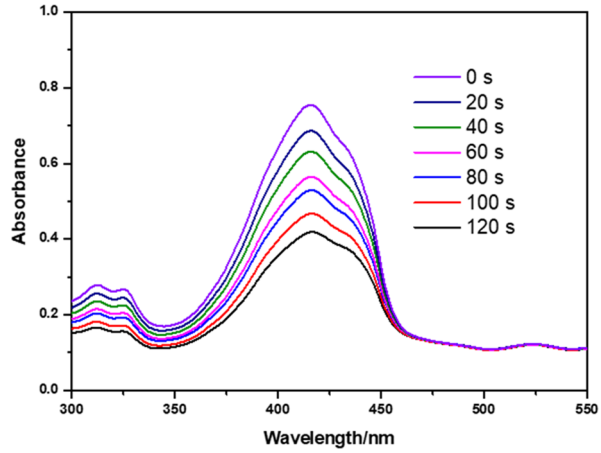

Figure 13. UV−vis spectra of the DPBF solution with 300 nm-PCN-224 under visible light.

3. CONCLUSIONS

In summary, this study demonstrated that PCN-224 with a size of 300 nm is an efficient material for TC and CIP removal in aqueous solutions. The adsorption kinetics, thermodynamics, and isotherms of TC and CIP were calculated to characterize the adsorption behavior of TC and CIP on 300 nm-PCN-224. The maximum adsorption capacity of 300 nm-PCN-224 is obtained as 354.81 mg g^{-1} for TC and 207.16 mg g^{-1} for CIP, which is comparatively very high in comparison with the reported literature. Mechanism analysis showed that the adsorption of TC and CIP molecule on 300 nm-PCN-224 is predominantly through electrostatic attraction, hydrogen bonding, and $\pi-\pi$ interactions. In addition, the adsorbent was easily regenerated by the photocatalytic method and can be reused for five cycles without significant performance deterioration. This study also provides useful information for the future research of highly efficient adsorbent materials, which can be used for the removal of antibiotic pollutants from wastewater.

4. EXPERIMENTAL SECTION

4.1. Preparation of PCN-224. The synthesis method is slightly modified on the basis of the previous report.[55]

For the synthesis of 150 nm-PCN-224, 5,10,15,20-tetrakis (4-carboxyphenyl) porphyrin (H_2TCPP) (0.1 g), zirconyl

https://doi.org/10.1021/acsomega.1c00919
ACS Omega 2021, 6, 17228−17238

chloride octahydrate ($ZrOCl_2 \cdot 8H_2O$) (0.3 g), and benzoic acid (BA) (2.8 g) were dissolved in 100 mL of *N*,*N*-dimethylformamide (DMF) in a 250 mL round-bottom flask and the mixture was stirred at 90 °C for 6 h. After the reaction was complete, the product was collected by centrifugation (14 000 rpm, 30 min), followed by washing with fresh DMF three times. The resulting sample was collected and dried overnight at 60 °C in a vacuum. The 500 nm-PCN-224 sample was synthesized in the same way, only by adjusting the amount of BA to 3.3 g and the centrifugal speed to 8000 rpm.

For the synthesis of 300 nm-PCN-224, $ZrOCl_2 \cdot 8H_2O$ (0.03 g), H_2TCPP (0.01 g), and BA (0.3 g) were ultrasonically mixed in a Pyrex tube containing 2.0 mL of DMF. After heating the mixture at 120 °C for 24 h, the obtained mixture was centrifuged at 10 000 rpm for 5 min. The obtained product was thoroughly washed with DMF three times and dried overnight at 60 °C in a vacuum. The 6 μm-PCN-224 sample was synthesized in the same way, except the amount of BA was adjusted to 0.6 g and the centrifugal speed to 8000 rpm.

4.2. Characterizations. X-ray diffraction (XRD) data were obtained on an X-ray diffractometer (SmartLab, Rigaku) operated at 40 kV and 30 mA with a Cu Kα X-ray radiation source. The morphological properties of PCN-224 powder were obtained using a SUPRA55 field emission scanning electron microscopy (FESEM). Fourier transform infrared (FT-IR) spectra were performed on a BRUKER-α FT-IR spectrometer. The N_2 adsorption−desorption isotherms were measured using a Micromeritics ASAP 2020 system at 77 K.

4.3. Adsorption Experiments. The adsorption capacity of the PCN-224 sample was determined by focusing on the two TC and CIP model antibiotic contaminants. The antibiotic stock was prepared by dissolving antibiotics in deionized water, from which all experimental antibiotic solutions were diluted. First, four PCN-224 samples of different sizes were used to adsorb TC and CIP to select the appropriate sample. Adsorption experiments were conducted at different time intervals for kinetic studies. Generally, 25 mg of adsorbent was added to 50 mL of antibiotic solution (10 mg L^{-1}), and the absorbance of 1 mL of supernatant was measured regularly at different time intervals until an equilibrium was reached. The maximum absorption wavelengths of TC and CIP were 357 and 278 nm, respectively. The adsorptive capacity (q_t, mg g^{-1}) and the adsorption efficiency (R) of the adsorbates on the adsorbent were calculated with the following equations

$$q_t = \frac{C_0 - C_t}{m} V \tag{9}$$

$$R = \frac{(C_0 - C_e)}{C_0} \times 100\% \tag{10}$$

where C_0 and C_t (mg L^{-1}) are the initial concentration and the concentration at each time interval, respectively, V (L) is the volume of the sulfanilamide solution, and m (g) is the mass of the adsorbent used. Equilibrium concentrations (C_e) and adsorption capacity (q_e) were measured by the above-mentioned method, and R is the adsorption efficiency.

The adsorption isotherm experiments were carried out in the initial concentration range of TC of 10−300 mg L^{-1} and CIP of 10−250 mg L^{-1}. Adsorption thermodynamics experiments were carried out at different temperatures (298, 308, 318 K). To investigate the effect of pH, 0.1 mol L^{-1} HCl and 0.1 mol L^{-1} NaOH were used to adjust their values to the desired pH range. In addition, NaCl (0−0.1 mol L^{-1}) was selected to investigate the effect of the ionic strength of the solution on the adsorption process.

4.4. Photocatalytic Regeneration of Adsorbent. The photocatalytic decomposition of antibiotics was performed in vials containing 1 mg of PCN-224 and 4 mL of antibiotic solution (30 ppm). After magnetically stirring for 1 h to achieve an adsorption−desorption equilibrium in the dark environment, the suspensions were irradiated by a 500 W Xe lamp with a 420 nm cutoff filter. The specific optical power density was 1000 W m^{-2} in the photodegradation experiment. After a period of exposure, the suspension solution was filtered by PVDF filters (0.45 μm), and then the PVDF filter was washed twice with 3 mL of ethanol, and the antibiotic concentration in the eluate was measured by a UV spectrophotometer. The photocatalytically regenerated PCN-224 was separated and dried in an oven for the consecutive cycles of TC and CIP adsorption.

4.5. DPBF Bleaching Experiment. The DPBF bleaching was performed in a cuvette containing 3 mL of DMF, 1.5 × 10^{-5} mol L^{-1} 300 nm-PCN-224, and 2.8 × 10^{-5} mol L^{-1} DPBF. The xenon lamp is used as the simulated light source, and the distance between the fixed light source and the cuvette is 15 cm, and the absorption spectrum of the solution after different irradiation times was recorded.

AUTHOR INFORMATION

Corresponding Authors

Jinjuan Xue − *School of Environmental and Safety Engineering, Changzhou University, Changzhou 213164, P. R. China*; orcid.org/0000-0001-6133-1581; Email: xuejinjuan@cczu.edu.cn

Mingxin Wang − *School of Environmental and Safety Engineering, Changzhou University, Changzhou 213164, P. R. China*; Email: wmx@cczu.edu.cn

Authors

Yuqing Zong − *School of Environmental and Safety Engineering, Changzhou University, Changzhou 213164, P. R. China*

Shuaishuai Ma − *College of Chemistry and Environmental Engineering, Jiangsu University of Technology, Changzhou 213001, P. R. China*; orcid.org/0000-0001-8394-1372

Jiamin Gao − *School of Environmental and Safety Engineering, Changzhou University, Changzhou 213164, P. R. China*

Minjing Xu − *School of Environmental and Safety Engineering, Changzhou University, Changzhou 213164, P. R. China*

Complete contact information is available at: https://pubs.acs.org/10.1021/acsomega.1c00919

Author Contributions

[§]Y.Z. and S.M. contributed equally to this work.

Notes

The authors declare no competing financial interest.

ACKNOWLEDGMENTS

This work was supported by the National Natural Science Foundation of China (grant nos. 21808019 and 41772240), the Natural Science Foundation of Jiangsu (grant nos. BK20180958 and BK20181048), the Science and Technology Bureau of Changzhou (CJ20190074), and the Postgraduate Research & Practice Innovation Program of Jiangsu Province (KYCX20_2594).

REFERENCES

(1) Rivera-Utrilla, J.; Sánchez-Polo, M.; Ferro-García, M. Á.; Prados-Joya, G.; Ocampo-Pérez, R. Pharmaceuticals as emerging contaminants and their removal from water. A review. *Chemosphere* **2013**, *93*, 1268−1287.

(2) Al-Khateeb, L. A.; Hakami, W.; Salam, M. A. Removal of non-steroidal anti-inflammatory drugs from water using high surface area nanographene: kinetic and thermodynamic studies. *J. Mol. Liq.* **2017**, *241*, 733−741.

(3) Talha, K.; Wang, B.; Liu, J.-H.; Ullah, R.; Feng, F.; Yu, J.; Chen, S.; Li, J.-R. Effective adsorption of metronidazole antibiotic from water with a stable Zr (IV)-MOFs: Insights from DFT, kinetics and thermodynamics studies. *J. Environ. Chem. Eng.* **2020**, *8*, No. 103642.

(4) Wang, H.; Yuan, X.; Wu, Y.; Zeng, G.; Dong, H.; Chen, X.; Leng, L.; Wu, Z.; Peng, L. In situ synthesis of In2S3@ MIL-125 (Ti) core−shell microparticle for the removal of tetracycline from wastewater by integrated adsorption and visible-light-driven photocatalysis. *Appl. Catal., B* **2016**, *186*, 19−29.

(5) Cui, Y.; Kang, W.; Qin, L.; Ma, J.; Liu, X.; Yang, Y. Ultrafast synthesis of magnetic hollow carbon nanospheres for the adsorption of quinoline from coking wastewater. *New J. Chem.* **2020**, *44*, 7490−7500.

(6) Balarak, D.; Azarpira, H. Photocatalytic degradation of Sulfamethoxazole in water: investigation of the effect of operational parameters. *Int. J. ChemTech Res.* **2016**, *9*, 731−738.

(7) Balarak, D.; Mostafapour, F. K.; Azarpira, H. Adsorption isotherm studies of tetracycline antibiotics from aqueous solutions by maize stalks as a cheap biosorbent. *Int. J. Pharm. Technol.* **2016**, *8*, 16664−16675.

(8) Ahmadi, S.; Banach, A.; Mostafapour, F. K.; Balarak, D. Study survey of cupric oxide nanoparticles in removal efficiency of ciprofloxacin antibiotic from aqueous solution: Adsorption isotherm study. *Desalin. Water Treat.* **2017**, *89*, 297−303.

(9) Azarpira, H.; Balarak, D. Rice husk as a biosorbent for antibiotic Metronidazole removal: Isotherm studies and model validation. *Int. J. ChemTech Res.* **2016**, *9*, 566−573.

(10) Van Doorslaer, X.; Dewulf, J.; Van Langenhove, H.; Demeestere, K. Fluoroquinolone antibiotics: an emerging class of environmental micropollutants. *Sci. Total Environ.* **2014**, *500−501*, 250−269.

(11) Balarak, D.; Azarpira, H.; Mostafapour, F. K. Study of the Adsorption Mechanisms of Cephalexin on to Azolla Filiculoides. *Der Pharm. Chem.* **2016**, *8*, 114−121.

(12) Mahvi, A. H.; Mostafapour, F. K.; Balarak, D. Biosorption Of Tetracycline From Aqueous Solution by Azolla Filiculoides: Equilibrium Kinetic And Thermodynamics Studies. *Fresenius Environ. Bull.* **2018**, *27*, 5759−5767.

(13) Sarker, M.; Bhadra, B. N.; Seo, P. W.; Jhung, S. H. Adsorption of benzotriazole and benzimidazole from water over a Co-based metal azolate framework MAF-5 (Co). *J. Hazard. Mater.* **2017**, *324*, 131−138.

(14) Husnain, S. M.; Asim, U.; Yaqub, A.; Shahzad, F.; Abbas, N. Recent trends of MnO_2-derived adsorbents for water treatment: a review. *New J. Chem.* **2020**, *44*, 6096−6120.

(15) Peng, X.; Hu, F.; Zhang, T.; Qiu, F.; Dai, H. Amine-functionalized magnetic bamboo-based activated carbon adsorptive removal of ciprofloxacin and norfloxacin: A batch and fixed-bed column study. *Bioresour. Technol.* **2018**, *249*, 924−934.

(16) Yang, W.; Lu, Y.; Zheng, F.; Xue, X.; Li, N.; Liu, D. Adsorption behavior and mechanisms of norfloxacin onto porous resins and carbon nanotube. *Chem. Eng. J.* **2012**, *179*, 112−118.

(17) Wang, B.; Jiang, Y.-s.; Li, F.-y.; Yang, D.-y. Preparation of biochar by simultaneous carbonization, magnetization and activation for norfloxacin removal in water. *Bioresour. Technol.* **2017**, *233*, 159−165.

(18) Liang, Z.; Zhaob, Z.; Sun, T.; Shi, W.; Cui, F. Adsorption of quinolone antibiotics in spherical mesoporous silica: Effects of the retained template and its alkyl chain length. *J. Hazard. Mater.* **2016**, *305*, 8−14.

(19) Wu, X.; Huang, M.; Zhou, T.; Mao, J. Recognizing removal of norfloxacin by novel magnetic molecular imprinted chitosan/γ-Fe_2O_3 composites: selective adsorption mechanisms, practical application and regeneration. *Sep. Purif. Technol.* **2016**, *165*, 92−100.

(20) Li, W.; Wang, J.; He, G.; Yu, L.; Noor, N.; Sun, Y.; Zhou, X.; Hu, J.; Parkin, I. P. Enhanced adsorption capacity of ultralong hydrogen titanate nanobelts for antibiotics. *J. Mater. Chem. A* **2017**, *5*, 4352−4358.

(21) Azarpira, H.; Mahdavi, Y.; Khaleghi, O.; Balarak, D. Thermodynamic Studies on the Removal of Metronidazole Antibiotic by Multi-Walled Carbon Nanotubes. *Der Pharm. Lett.* **2016**, *8*, 114−121.

(22) Mirsoleimani-azizi, S. M.; Setoodeh, P.; Zeinali, S.; Rahimpour, M. R. Tetracycline antibiotic removal from aqueous solutions by MOF-5: Adsorption isotherm, kinetic and thermodynamic studies. *J. Environ. Chem. Eng.* **2018**, *6*, 6118−6130.

(23) Zhou, H.-C.; Long, J. R.; Yaghi, O. M. Introduction to metal−organic frameworks. *Chem. Rev.* **2012**, *112*, 673−674.

(24) Cao, C.-S.; Shi, Y.; Xu, H.; Zhao, B. A multifunctional MOF as a recyclable catalyst for the fixation of CO_2 with aziridines or epoxides and as a luminescent probe of Cr (VI). *Dalton Trans.* **2018**, *47*, 4545−4553.

(25) Gao, Y.; Kang, R.; Xia, J.; Yu, G.; Deng, S. Understanding the adsorption of sulfonamide antibiotics on MIL-53s: Metal dependence of breathing effect and adsorptive performance in aqueous solution. *J. Colloid Interface Sci.* **2019**, *535*, 159−168.

(26) Barea, E.; Montoro, C.; Navarro, J. A. Toxic gas removal-metal−organic frameworks for the capture and degradation of toxic gases and vapours. *Chem. Soc. Rev.* **2014**, *43*, 5419−5430.

(27) Gao, Y.; Yu, G.; Liu, K.; Wang, B. Luminescent mixed-crystal Ln-MOF thin film for the recognition and detection of pharmaceuticals. *Sens. Actuators, B* **2018**, *257*, 931−935.

(28) Chen, Y.-Z.; Wang, Z. U.; Wang, H.; Lu, J.; Yu, S.-H.; Jiang, H.-L. Singlet oxygen-engaged selective photo-oxidation over Pt nanocrystals/porphyrinic MOF: the roles of photothermal effect and Pt electronic state. *J. Am. Chem. Soc.* **2017**, *139*, 2035−2044.

(29) DeRosa, M. C.; Crutchley, R. J. Photosensitized singlet oxygen and its applications. *Coord. Chem. Rev.* **2002**, *233−234*, 351−371.

(30) Gao, Y.; Xia, J.; Liu, D.; Kang, R.; Yu, G.; Deng, S. Synthesis of mixed-linker Zr-MOFs for emerging contaminant adsorption and photodegradation under visible light. *Chem. Eng. J.* **2019**, *378*, No. 122118.

(31) Chen, M.; Long, Z.; Dong, R.; Wang, L.; Zhang, J.; Li, S.; Zhao, X.; Hou, X.; Shao, H.; Jiang, X. Titanium Incorporation into Zr-Porphyrinic Metal−Organic Frameworks with Enhanced Antibacterial Activity against Multidrug-Resistant Pathogens. *Small* **2020**, *16*, No. 1906240.

(32) Feng, D.; Chung, W.-C.; Wei, Z.; Gu, Z.-Y.; Jiang, H.-L.; Chen, Y.-P.; Darensbourg, D. J.; Zhou, H.-C. Construction of ultrastable porphyrin Zr metal−organic frameworks through linker elimination. *J. Am. Chem. Soc.* **2013**, *135*, 17105−17110.

(33) Han, D.; Han, Y.; Li, J.; Liu, X.; Yeung, K. W. K.; Zheng, Y.; Cui, Z.; Yang, X.; Liang, Y.; Li, Z.; et al. Enhanced photocatalytic activity and photothermal effects of cu-doped metal−organic frameworks for rapid treatment of bacteria-infected wounds. *Appl. Catal., B* **2020**, *261*, No. 118248.

(34) Wang, L.; Jin, P.; Huang, J.; She, H.; Wang, Q. Integration of copper (II)-porphyrin zirconium metal−organic framework and titanium dioxide to construct Z-scheme system for highly improved photocatalytic CO2 reduction. *ACS Sustainable Chem. Eng.* **2019**, *7*, 15660−15670.

(35) Shi, L.; Yang, L.; Zhang, H.; Chang, K.; Zhao, G.; Kako, T.; Ye, J. Implantation of iron (III) in porphyrinic metal organic frameworks for highly improved photocatalytic performance. *Appl. Catal., B* **2018**, *224*, 60−68.

(36) Leofanti, G.; Padovan, M.; Tozzola, G.; Venturelli, B. Surface area and pore texture of catalysts. *Catal. Today* **1998**, *41*, 207−219.

(37) Xiong, W.; Zeng, Z.; Li, X.; Zeng, G.; Xiao, R.; Yang, Z.; Xu, H.; Chen, H.; Cao, J.; Zhou, C.; Qin, L. Ni-doped MIL-53 (Fe)

https://doi.org/10.1021/acsomega.1c00919
ACS Omega 2021, 6, 17228−17238

nanoparticles for optimized doxycycline removal by using response surface methodology from aqueous solution. *Chemosphere* **2019**, *232*, 186−194.
(38) Yang, Z.-h.; Cao, J.; Chen, Y.-p.; Li, X.; Xiong, W.-p.; Zhou, Y.-y.; Zhou, C.-y.; Xu, R.; Zhang, Y.-r. Mn-doped zirconium metal-organic framework as an effective adsorbent for removal of tetracycline and Cr (VI) from aqueous solution. *Microporous Mesoporous Mater.* **2019**, *277*, 277−285.
(39) Xiong, W.; Zeng, Z.; Li, X.; Zeng, G.; Xiao, R.; Yang, Z.; Zhou, Y.; Zhang, C.; Cheng, M.; Hu, L.; et al. Multi-walled carbon nanotube/amino-functionalized MIL-53 (Fe) composites: remarkable adsorptive removal of antibiotics from aqueous solutions. *Chemosphere* **2018**, *210*, 1061−1069.
(40) Li, X.; Yuan, H.; Quan, X.; Chen, S.; You, S. Effective adsorption of sulfamethoxazole, bisphenol A and methyl orange on nanoporous carbon derived from metal−organic frameworks. *J. Environ. Sci.* **2018**, *63*, 250−259.
(41) Shi, S.; Fan, Y. W.; Huang, Y. M. Facile Low Temperature Hydrothermal Synthesis of Magnetic Mesoporous Carbon Nanocomposite for Adsorption Removal of Ciprofloxacin Antibiotics. *Ind. Eng. Chem. Res.* **2013**, *52*, 2604−2612.
(42) Zhang, D.; He, Q.; Hu, X.; Zhang, K.; Chen, C.; Xue, Y. Enhanced adsorption for the removal of tetracycline hydrochloride (TC) using ball-milled biochar derived from crayfish shell. *Colloids Surf., A* **2021**, *615*, No. 126254.
(43) Guo, Y.; Yan, C. C.; Wang, P. F.; Rao, L.; Wang, C. Doping of carbon into boron nitride to get the increased adsorption ability for tetracycline from water by changing the pH of solution. *Chem. Eng. J.* **2020**, *387*, No. 124136.
(44) Nassar, M. Y.; Ahmed, I. S.; Raya, M. A. A facile and tunable approach for synthesis of pure silica nanostructures from rice husk for the removal of ciprofloxacin drug from polluted aqueous solutions. *J. Mol. Liq.* **2019**, *282*, 251−263.
(45) Mengting, Z.; Kurniawan, T. A.; Avtar, R.; Othman, M. H. D.; Ouyang, T.; Huang, Y. J.; Zhang, X. T.; Setiadi, T.; Iswanto, I. Applicability of TiO_2(B) nanosheets@hydrochar composites for adsorption of tetracycline (TC) from contaminated water. *J. Hazard. Mater.* **2021**, *405*, No. 123999.
(46) Carabineiro, S. A. C.; Thavorn-amornsri, T.; Pereira, M. F. R.; Serp, P.; Figueiredo, J. L. Comparison between activated carbon, carbon xerogel and carbon nanotubes for the adsorption of the antibiotic ciprofloxacin. *Catal. Today* **2012**, *186*, 29−34.
(47) Hao, R.; Xiao, X.; Zuo, X. X.; Nan, J. M.; Zhang, W. D. Efficient adsorption and visible-light photocatalytic degradation of tetracycline hydrochloride using mesoporous BiOI microspheres. *J. Hazard. Mater.* **2012**, *209−210*, 137−145.
(48) Yu, J.; Xiong, W.; Li, X.; Yang, Z.; Cao, J.; Jia, M.; Xu, R.; Zhang, Y. Functionalized MIL-53 (Fe) as efficient adsorbents for removal of tetracycline antibiotics from aqueous solution. *Microporous Mesoporous Mater.* **2019**, *290*, No. 109642.
(49) Peng, H.; Cao, J.; Xiong, W.; Yang, Z.; Jia, M.; Sun, S.; Xu, Z.; Zhang, Y.; Cai, H. Two-dimension N-doped nanoporous carbon from KCl thermal exfoliation of Zn-ZIF-L: Efficient adsorption for tetracycline and optimizing of response surface model. *J. Hazard. Mater.* **2021**, *402*, No. 123498.
(50) Chen, J.-J.; Wang, L.-J.; Xu, G.-J.; Wang, X.; Zhao, R.-S. Highly Stable Zr (IV)-Based Porphyrinic Metal−Organic Frameworks as an Adsorbent for the Effective Removal of Gatifloxacin from Aqueous Solution. *Molecules* **2018**, *23*, No. 937.
(51) Xiong, W.; Zeng, Z.; Zeng, G.; Yang, Z.; Xiao, R.; Li, X.; Cao, J.; Zhou, C.; Chen, H.; Jia, M.; et al. Metal−organic frameworks derived magnetic carbon-αFe/Fe_3C composites as a highly effective adsorbent for tetracycline removal from aqueous solution. *Chem. Eng. J.* **2019**, *374*, 91−99.
(52) Al-Ghouti, M. A.; Khraisheh, M. A. M.; Allen, S. J.; Ahmad, M. N. The removal of dyes from textile wastewater: a study of the physical characteristics and adsorption mechanisms of diatomaceous earth. *J. Environ. Manage.* **2003**, *69*, 229−238.
(53) Jiang, L. H.; Liu, Y. G.; Zeng, G. M.; Xiao, F. Y.; Wang, X. J.; et al. Removal of 17 beta-estradiol by few-layered graphene oxide nanosheets from aqueous solutions: External influence and adsorption mechanism. *Chem. Eng. J.* **2016**, *284*, 93−102.
(54) Du, C.; Zhang, Z.; Yu, G.; Wu, H.; Chen, H.; Zhou, L.; Zhang, Y.; Su, Y.; Tan, S.; Yang, L.; et al. A review of metal organic framework (MOFs)-based materials for antibiotics removal via adsorption and photocatalysis. *Chemosphere* **2021**, *272*, No. 129501.
(55) Park, J.; Jiang, Q.; Feng, D.; Mao, L.; Zhou, H.-C. Size-controlled synthesis of porphyrinic metal−organic framework and functionalization for targeted photodynamic therapy. *J. Am. Chem. Soc.* **2016**, *138*, 3518−3525.

https://doi.org/10.1021/acsomega.1c00919
ACS Omega 2021, 6, 17228−17238